Applied Thermal Engineering 221 (2023) 119866

Contents lists available at ScienceDirect

Applied Thermal Engineering

journal homepage: www.elsevier.com/locate/apthermeng

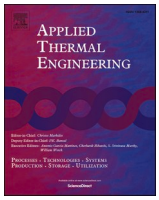

Research Paper

Design optimization of plate-fin heat sink with forced convection for single-module thermoelectric generator

Toni Pujol [a,*], Ilya T'Jollyn [b,c], Eduard Massaguer [a], Albert Massaguer [a], Ivan R. Cózar [a], Michel De Paepe [b,c]

[a] Department of Mechanical Engineering and Industrial Construction, University of Girona, 17003 Girona, Spain
[b] Department of Electromechanical, Systems and Metal Engineering, Ghent University, 9000 Gent, Belgium
[c] Flanders Make Core Lab EEDT-MP, Flanders Make, 3000 Leuven, Belgium

ARTICLE INFO

Keywords:
TEG
Heat sink design
Net power
Forced convection

ABSTRACT

Thermoelectric generators (TEGs) often use plate-fin heat sinks as cold side heat exchangers under forced convection. The available net electrical power obtained from these TEGs corresponds to that generated (Seebeck effect) minus that consumed (cooling fan). Generation and self-consumption have different trends as a function of the air flow speed, so a maximum of the net electrical power is expected when varying the cooling flow rate. Here, a semi-analytical model was developed to predict the maximum net electrical power of a single TEG module with a plate-fin heat sink with non-bypassed forced convection. The model was successfully validated with experimental data. It was applied to determine the heat sink design (fin thickness and fin-to-fin distance) that optimized the net electrical power for given values of hot source temperature, TEG properties, and duct cross-section. Numerical results indicated that the optimal dimensions of the plate-fin heat sink depended, among others, on the TEG effective properties. For a given TEG, the net output power was less sensitive to changes in fin thickness than in fin spacing. The optimal heat sink designs predicted by the model for the cases studied had fin thicknesses of 0.32 and 0.44 mm with fin-to-fin distances of 1 mm.

1. Introduction

Thermoelectric generators (TEGs) are solid-state devices that installed in between a hot source and a cold sink produce electrical energy due to the Seebeck effect [1]. Commercial thermoelectric modules for electric power generation are a mature technology especially suitable for the niche market of low power devices in off-grid applications [2]. Apparatus located in extreme environments as well as autonomous sensors are examples in which TEGs have successfully been applied [3–4].

Recently, TEGs have gained interest in cooling applications of electronic devices either by providing electric energy to other cooling technologies (indirect use) or by working as self-cooling units (direct use) [5]. As an indirect use, several proposals have employed TEGs as energy sources to drive thermoelectric coolers (TECs) in combined TEC-TEG systems [6]. Large improvements in cooling capacities (75 % increase) of TEC-TEG systems when adopting a simple redesign of a combined TEC-TEG configuration have been reported [6]. In a direct use, the TEG hot side is attached to the target hot source, whereas the TEG cold side is in contact with a heat sink whose forced flow is driven by a fan or a pump electrically powered by its own TEG [5,7]. These types of self-cooling devices may reach very low values of thermal resistances ($<0.5\ K\ W^{-1}$) [8]. Martinez et al. [9] obtained reductions of the source-to-ambient thermal resistance on the order of 30 % when installing TEGs in between a heat pipe exchanger and the hot source so as to shift the convection mode from natural to self-forced. In comparison, self-cooling TEGs with plate-fin heat exchangers under forced convection [7,8] reached efficiency values slightly below those found without TEGs and with heat pipes under natural convection [9].

However, simple plate-fin heat exchangers may substantially increase their performances when adopting designs specifically optimized for a given application [10]. Knight et al. [11] developed an analytical model for plate-fin heat sinks under forced convection to determine the fin to channel width that produced the lowest thermal resistance, with results being confirmed from experimental tests [12]. Teertstra et al. [13] proposed a composite solution of both fully developed and developing flows in the channels between fins for a forced convection heat sink model, whose predictions agreed well with observations. Bejan and Morega [14] extended the analysis to three dimensions by studying pin

* Corresponding author.
E-mail address: toni.pujol@udg.edu (T. Pujol).

https://doi.org/10.1016/j.applthermaleng.2022.119866
Received 30 June 2022; Received in revised form 21 November 2022; Accepted 11 December 2022
Available online 16 December 2022

Nomenclature

A	cross-sectional area (m^2)
a	coefficient of the fin thickness power fitting (m)
b	heat sink base height (m), exponent term of the fin thickness power fitting (-)
c_p	air specific heat (J K^{-1} kg^{-1})
d	fin-to-fin distance (m)
D_h	hydraulic diameter (m)
f_{app}	apparent friction coefficient (-)
f_{tur}	turbulent friction coefficient (-)
H	fin height (m)
k	thermal conductivity (W m^{-1} K^{-1})
K_c	minor loss coefficient at heat sink inlet (-)
K_e	minor loss coefficient at heat sink outlet (-)
L	heat sink length (m)
L^+	dimensionless heat sink length for pressure drop calculation (-)
L^*	dimensionless heat sink length for heat transfer calculation (-)
N	number of samples (-)
n	number of fins (-)
$Nu_{m,T}$	Nusselt number for an isothermal fin array (-)
P_{hy}	hydraulic power (W)
P_n	net output power at P_{TEG} conditions (W)
P_{nopt}	optimal net output power (maximum of all $P_{nopt,n}$ = maximum net output power with unconstrained t, d, v and R_L) (W)
$P_{nopt,n}$	maximum of P_{nmax,vR_L} cases with fin number n (W)
P_{nmax,dvR_L}	maximum net output power with unconstrained d, v and R_L (W)
P_{nmax,vR_L}	maximum net output power with unconstrained v and R_L (W)
P_{TEG}	maximum TEG output power with unconstrained R_L (W)
Δp	pressure drop through the heat sink (Pa)
Pr	Prandtl number (-)
Q	heat transfer rate (W)
Q_i	heat transfer rate of an isothermal fin (W)
R	thermal resistance (K W^{-1})
R_i	TEG electrical internal resistance (Ω)
R_L	TEG electrical load resistance (Ω)
R_t	total thermal resistance (K W^{-1})
Re	Reynolds number (-)
T	temperature (°C)
ΔT	temperature difference (°C)
ΔT_{HSmax}	heat sink maximum temperature difference (°C)
t	fin thickness (m)
TEG	thermoelectric generator
v	air flow velocity (m s^{-1})
$\dot{V}$	volumetric flow rate (m^3 s^{-1})
W	heat sink width (m)
x	thickness of the material (m)
$z_{0.025}$	value of the normal distribution at the 95 % confidence level (-)
α	effective Seebeck coefficient factor (V K^{-1})
β	momentum correction factor (-)
ε_e	uncertainty due to the measurement equipment
ε_s	uncertainty due to the analysis of the data series
ε_t	total uncertainty
η	fin efficiency (-)
Ξ	fan efficiency (-)
μ	air absolute viscosity (Pa s)
ν	air kinematic viscosity (m^2 s^{-1})
ρ	air density (kg m^{-3})
σ	fraction of frontal free flow area (-)
σ_{st}	standard deviation
φ	friction factor correction term (-)

Subscripts

a	ambient air
ac	aluminum – ceramic (for contact resistance)
c	TEG cold side
cd	conduction
ct	contact
$cTEG$	ceramic – TEG (for contact resistance)
cv	convection
h	TEG hot side
HS	heat sink
opt	optimal
p	hot source
$TEGHS$	TEG – heat sink (for contact resistance)

fins and staggered parallel-plate fins geometries, the latter found to reach thermal resistances half of those for continuous plate-fin heat sinks. Bejan [15] considered the entropy generation minimization method to account for both thermal and fluid effects to optimize the geometry of heat exchangers. This optimization technique was applied by Culham and Muzychka [16] to plate-fin heat sinks, and analyzed several cases while increasing the number of unconstrained parameters. For a heat sink with dimensions of 50 × 50 × 25 mm (wide × long × high) and a total heat dissipation of 30 W, the optimal fin thickness was 0.4×10^{-3} m, with 27 number of fins, and an average air flow velocity of 2.81 m s^{-1}. Later, Bar-Cohen et al. [17] introduced the least-energy optimization technique that also took into account the energy used in the operation and fabrication of the heat sink. These authors analyzed air-cooled heat sinks for both natural (plate-fin and pin fin designs) and forced (pate-fin design) convection concluding that the achievement of the maximum thermal performance required fins with high aspect ratio. For forced convection plate-fin heat sinks of dimensions 100 × 100 × 50 mm (wide × long × high), with 20 Pa pressure drop, and 0.2 W pumping power, the least material designs needed 0.12×10^{-3} m thick fins, and the maximum heat transfer design needed 0.57×10^{-3} m thick fins. Plate-fin heat sink designs from multi-objective optimization with simultaneous minimization of both the entropy generation rate and the material cost of the heat sink have also been obtained by Chen and Chen [18]. The optimal geometry found under a heat load of 30 W for a heat sink of dimensions 50 × 50 mm (wide × long) used 1.0×10^{-3} m fin thickness, 1.6×10^{-3} m fin-to-fin distance, and 12×10^{-3} m height [18]. For complex designs, computational fluid dynamics (CFD) techniques have been used to optimize heat sink geometries since no analytical expressions for both thermal and fluid flow behavior are available. Thus, for example, Gondipali et al. [19] optimized the geometry of parallel plate heat sinks with removed material near the center of the plates so as to enhance the airflow at that location. Al-Damook et al. [20] optimized the geometry of pin heat sinks with rectangular slots and with notches including fan power consumption and heat sink mass requirements. By applying an artificial neural network to data obtained from CFD results of a plate-fin heat sink with constant width, length and height (37 × 68 × 25 mm), Pragadeesh et al. [21] obtained an optimum heat transfer when the fin thickness was equal to 0.25×10^{-3} m. Recently, Özdilli and Şevik [22] and Şevik and Özdilli [23] improved the thermal resistance of standard parallel plate heat sinks by developing two types of trapezoidal

curved with dolphin fins heat sinks and of standard cross cut parallel plate heat sinks by splaying some of the fins, respectively.

Plate-fin heat sinks have been widely adopted in TEGs for their simplicity and cost-effectiveness. Rattner and Meehan [24] have recently modeled a system composed of an array of commercial TEG modules that use plate-fin heat sinks that dissipated heat to the ambient air. They found that the sensitivity of the output power to changes in the value of the heat transfer coefficient at the cold side was almost twice the sensitivity to changes in the overall heat transfer coefficient at the hot side. Therefore, a proper design of the cold side heat exchanger becomes essential in TEG applications.

In addition, the power required to move the forced flow through the cold side heat exchanger must be subtracted to the output power generated by the TEG in order to determine the available net output power that can be extracted from a TEG device [25–26]. In a TEG module attached to a hot reservoir, an increase in the forced flow through the heat sink decreases the cold side thermal resistance leading to an increase in the TEG power generation. However, since the amount of energy consumed to drive the flow increases non-linearly with the flow rate, the TEG net output power reaches a maximum at intermediate values of the flow rate.

Different strategies are applied to increase this TEG net output power. Several are focused on improving the TEG output power by developing new thermoelectric materials, redesigning the geometrical dimensions of both *p*-type and *n*-type legs, applying pulsed heat fluxes, etc. (see, e.g., [27–29]). Others, for example, are aimed at boosting the heat transfer rate by modifying the design of the heat exchangers. Many studies have focused on optimizing the geometry of the hot side heat exchanger. For example, Martinez et al. [30] obtained the optimal length of fins and the fin-to-fin distance for a plate-fin heat exchanger located at the hot side of the TEG. Najjar and Sallam [31] applied a genetic algorithm to find the dimensions of the hot side heat exchanger that maximized the net output power in an automotive TEG. For a copper rectangular offset strip fin heat exchanger with 708 °C gas temperature and 21.9 g s^{-1} flow rate, the optimal dimensions were 0.12 $\times$ 10^{-3} m for fin thickness and 3.97 $\times$ 10^{-3} m for the fin-to-fin distance [31]. Also for automotive TEGs, Kempf and Zhang [32] included the material properties in the optimization process, Wang et al. [33] analyzed the effect of using different geometries and distributions of fins, both focusing on the hot side heat exchanger, and He et al. [34] found the overall width, length and height of the hot side heat exchanger that maximized the TEG power. Multi-objective optimization (power output, pumping power, number of thermoelectric modules, and volume of heat exchanger) has also been proposed with TEG modules located between cold and hot side heat exchangers shaped with triangular channels [35]. For plate-fin heat exchangers, Ji et al. [36] obtained the length and material that maximized the TEG output power via the Taguchi method, and Tian et al. [37] deduced the cold to hot heat exchangers surface ratio that maximized the TEG efficiency, although both studies did not find the best values of fin thickness and/or fin-to-fin distance. The effect of varying the geometry of the cold side heat sink on the TEG output power was analyzed by Comamala et al. [38] in a cooling water system with tube heat exchangers. CFD analyses have been applied to determine the hot side heat exchanger configuration (plate vs pin fin ones) for a TEG formed with a single thermoelectric module that provided the maximum net output power, though by assuming a pump efficiency equal to 1 [39].

In comparison with these previous studies, the present work focused on a single TEG module with constant temperature at the hot source, and air forced convection in the cold heat exchanger with no bypass. These conditions were already analyzed by T'Jollyn et al. [40], although with a simplified model without experimental validation nor a thorough optimization process. Thus, the purpose here was to determine the plate-fin heat sink geometry (fin thickness and fin-to-fin distance) that optimized the net output power for given values of the TEG properties, fan efficiency, duct cross-sectional area, and hot source temperatures. The methodology consisted of 1) developing a hydraulic, thermal, and electrical analytical model of a single commercial TEG module attached to a plate-fin heat sink, 2) validating the numerical model with experimental data, 3) applying the model to find both fin-to-fin distance and fin thickness of the heat sink that provided a maximum in the TEG net output power for different hot source temperatures, 4) discussing the practical consequences of the results found, including additional experimental data to confirm the geometrical conditions for the optimal point.

The structure of the paper is as follows. Section 2 describes the analytical model based on the plate-fin heat sink model of Lindstedt and Karvinen [41] that here included additional elements as, for example, a TEG module. Section 3 details the validation procedure of the numerical model with experimental data obtained with an aluminum plate-fin heat sink. The results obtained when changing the geometrical parameters of the plate-fin heat sink are shown in Section 4, where the optimal design in terms of the TEG net output power was found for different conditions of the hot source. These numerical predictions were tested with a different heat sink with an almost optimal geometrical configuration. Finally, the main conclusions are listed in Section 5.

2. Analytical model

2.1. TEG device and heat sink

The TEG device used is schematically shown in Fig. 1. It reproduced the experimental set up employed in Section 3. Essentially, a hot plate at the bottom heated a rectangular aluminum block that, in its upper face, was in contact with a ceramic plate of known thermal conductivity. The cold side of this ceramic plate was also in contact with the hot side of a commercial TEG module of equal cross-sectional area. Finally, the cold side of the TEG was in contact with the base of a plate-fin heat sink (see Fig. 1). The cooling method was of forced convection obtained by inserting the heat sink inside a square cross-sectional channel in which the flow was driven by a fan. The main assumptions of the numerical model explained below were: 1) no bypassing flow, 2) uniform velocity of the incoming air, 3) constant thermal properties, 4) non-isothermal fins, 5) adiabatic fin tips, 6) no heat flow losses to the environment, 7) constant effective Seebeck coefficient, 8) uniform temperatures at both TEG sides, 9) TEG power generation very small in comparison with the heat transfer rate (i.e., no change of the heat transfer rate across the TEG), 10) constant fan efficiency. Though some of the previous assumptions may limit the applicability of the model to reproduce real TEG device conditions, the procedure below may become useful to propose designs with high values of net extracted power.

2.2. Hydraulic model

The hydraulic model was based on Lindstedt and Karvinen [41] and on Kays and London [42]. The pressure drop through the heat sink Δp was calculated from a common formulation that assumes a series pressure drop,

$$\Delta p = \frac{1}{2}\rho v^2 \left(K_c + 4L^+ f_{app} Re + K_e\right) \quad (1)$$

where ρ was the air density and v was the average air velocity in the channel between fins. K_c and K_e were the minor loss coefficients at the contraction zone (flow entering the heat sink) and at the expansion zone (flow exiting the heat sink), respectively.

Primary losses of the flow within the heat sink were evaluated by the $\frac{1}{2}\rho v^2 4L^+ f_{app} Re$ term in Eq. (1). The Reynolds number Re of the flow within the heat sink was obtained from

$$Re = \frac{v D_h}{\nu} \quad (2)$$

where ν was the air kinematic viscosity (=1.56 $\times$ 10^{-5} m^2 s^{-1}; fluid

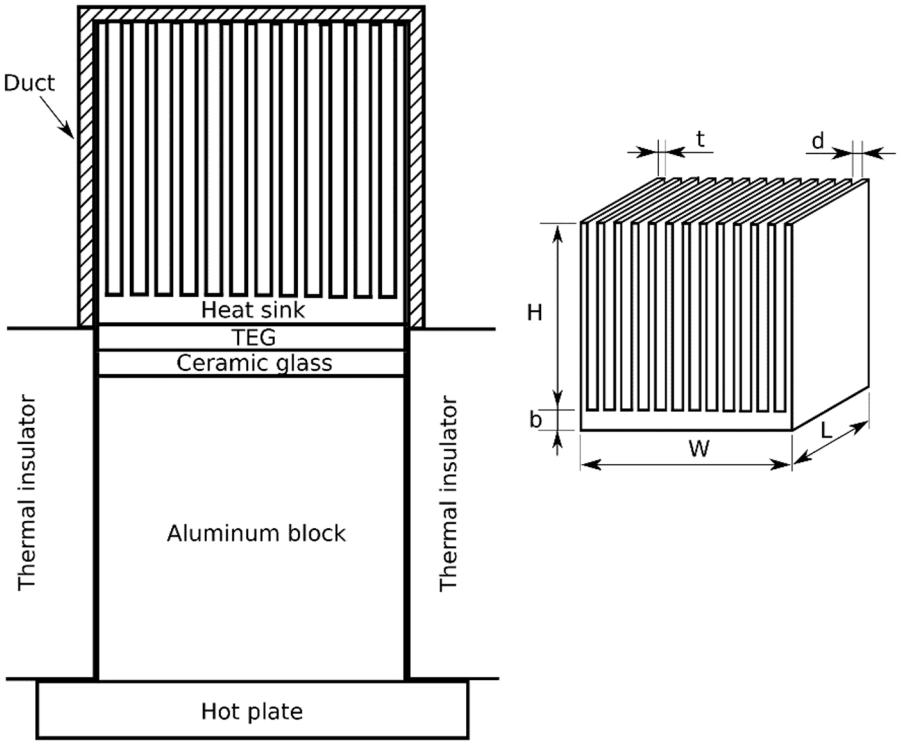

Fig. 1. (a) Schematics of the TEG system analyzed and (b) plate-fin heat sink main dimensions.

properties assumed constant for simplicity) and D_h was the hydraulic diameter equal to $2Hd/(d+H)$ with H and d the fin height and the fin-to-fin distance, respectively (see Fig. 1). For a laminar flow in the channel between fins (i.e., $Re < Re_{cr}$ with $Re_{cr} = 2300$, being chosen equal to that for the thermal model), the value of L^+ and $f_{app}Re$ followed an equation that combined both the asymptotic solution for an entry flow and that for a fully developed one (see [41]),

$$L^+ = \frac{L}{D_h Re}, f_{app}Re = \left[\left(\frac{3.44}{\sqrt{L^+}}\right)^2 + \left(\frac{24}{\varphi}\right)^2\right]^{\frac{1}{2}} \tag{3}$$

with L the heat sink length (Fig. 1), and where the φ function was defined as

$$\varphi = \left(1+\frac{d}{H}\right)^2\left[1-\frac{192}{\pi^5}\frac{d}{H}tanh\left(\frac{\pi}{2}\frac{H}{d}\right)\right] \tag{4}$$

From Kays and London [42], the minor loss coefficients in Eq. (1) were calculated as

$$K_c = 0.4\left(2-\sigma^2\right), K_e = 1+\sigma^2-2\beta\sigma \tag{5}$$

with

$$\sigma = \frac{d}{d+t}, \beta = 1+\left[\left(4.224\sqrt{L^+}\right)^{-2.7} + 0.2^{-2.7}\right]^{-\frac{1}{2.7}} \tag{6}$$

where t was the fin thickness (Fig. 1).

For turbulent flows ($Re > Re_{cr}$), the primary losses term $4L^+f_{app}Re$ in Eq. (1) was substituted by $(f_{tur}L)/D_h$, with the turbulent friction coefficient f_{tur} being,

$$f_{tur} = 0.0791\left(\frac{2\varphi Re}{3}\right)^{-\frac{1}{4}} \tag{7}$$

and with both contraction and expansion minor loss coefficients as [42],

$$K_c = 0.4\left(1-\sigma^{2.1}\right), K_e = 1+\sigma^2-2\sigma. \tag{8}$$

The vast majority of cases analyzed, however, had Re values below 1000, including the optimal designs discussed in Section 4.

2.3. Thermal model

The thermal model was simplified as an equivalent system of thermal resistances in series. Thus, the heat transfer rate Q through the system was assumed equal to

$$Q = \frac{T_p - T_a}{R_{ct,ac} + R_{cd,c} + R_{ct,cTEG} + R_{cd,TEG} + R_{ct,TEGHS} + R_{cv,HS}} \tag{9}$$

with T_p the temperature at the hot source (top of the aluminum block in Fig. 1) and T_a the ambient temperature of the incoming flow. All contact resistances of unit area were chosen constant and equal to 10^{-4} m^2 K W^{-1} that divided by the contact area A gave the absolute contact resistance R_{ct}, being in agreement with previous studies with TEG models [43]. The thermal resistance by conduction of the ceramic material ($R_{cd,c}$) and of the whole TEG module ($R_{cd,TEG}$) were calculated from $R_{cd,i} = x_i/(A_i k_i)$ for $i = c, TEG$, with x the thickness of the material, A its cross-sectional area and k its thermal conductivity. The effective values of these parameters for the commercial TEG module are evaluated in Section 3. The convective thermal resistance for the whole heat sink under forced convection ($R_{cv,HS}$) followed [41],

$$R_{cv,HS} = \frac{\Delta T_{HSmax}}{nQ_i\eta} \tag{10}$$

where ΔT_{HSmax} was the heat sink maximum temperature difference (average base plate-fin heat sink temperature minus incoming air temperature T_a), Q_i was the heat transfer rate of a geometrically identical isothermal fin, η was the fin efficiency defined as the ratio of the real heat transfer rate Q to Q_i, and n was the number of fins.

The ratio $Q_i/\Delta T_{HSmax}$ was expressed as

$$\frac{Q_i}{\Delta T_{HSmax}} = \rho c_p v Hd\left[1-exp\left(-4L^* Nu_{m,T}\right)\right] \tag{11}$$

with c_p the air specific heat (=1007 J K^{-1} kg^{-1}), $Nu_{m,T}$ the Nusselt

number for an isothermal fin array, and L^* a non-dimensional length. These last two terms for a laminar flow between the channels of the heat sink were

$$L^* = \frac{L}{D_h Re Pr} \tag{12}$$

$$Nu_{m,T} = 7.55 + \frac{0.024 L^{*-1.14}}{1 + 0.0358 \mathrm{Pr}^{0.17} L^{*-0.64}} \tag{13}$$

with the Prandlt number $Pr = (\mu c_p)/k_a$, and μ (=1.85 × 10^{-5} Pa s) and k_a (=0.02553 W m^{-1} K^{-1}) the air absolute viscosity and air thermal conductivity, respectively.

The fin efficiency value in Eq. (10) followed

$$\eta = \frac{tanh\left\{\sqrt{\frac{\left[1-\exp\left(-4L^* Nu_{m,T}\right)\right]k_a H^2}{4L^* k_{HS} dt}}\right\}}{\sqrt{\frac{\left[1-\exp\left(-4L^* Nu_{m,T}\right)\right]k_a H^2}{4L^* k_{HS} dt}}} \tag{14}$$

with k_{HS} the heat sink thermal conductivity (equal to 210 W m^{-1} K^{-1} and 398 W m^{-1} K^{-1} for the aluminum and copper heat sinks that were tested, respectively).

For a turbulent flow, Eq. (13) was substituted by

$$Nu_{m,T} = \frac{\frac{f_{tur}}{2}(Re - 1000)Pr}{1 + 12.7\sqrt{f_{tur}/2}\left(Pr^{2/3} - 1\right)}\left[1 + \left(\frac{D_h}{L}\right)^{2/3}\right] \tag{15}$$

Note that the assumptions of 1) no heat losses through the packing system and 2) a generation of energy by the TEG very small in comparison with the heat flux Q were implicit in Eq. (9). The latter approximation has recently been applied in analytical studies of TEG maximum power under different constraints at both hot and cold reservoirs (constant temperature vs constant heat fluxes [44]). This assumption was reasonable due to the low efficiency of commercial thermoelectric generator modules (in our case, below < 2 %).

2.4. TEG net output power

The maximum power generated by a TEG constrained to constant temperatures at its both hot and cold sides is attained when the electrical load resistance R_L matches the internal one R_i [45], being

$$P_{TEG} = \alpha^2 \frac{\left(T_{TEG,h} - T_{TEG,c}\right)^2}{4R_i} \tag{16}$$

where α is the effective Seebeck coefficient for the entire commercial module, and $T_{TEG,h}$ and $T_{TEG,c}$ are the TEG temperatures at its hot and cold sides, respectively.

However, the conditions applied to the case here studied were slightly different. In the TEG analyzed in Fig. 1, constant temperature at the hot source and constant flow conditions at the cold sink (temperature and volumetric flow rate of the convective air) were applied. Therefore, the maximum power generated by the TEG was not strictly reached at $R_L = R_i$, although the error of assuming Eq. (16) was expected to be<5 % due to the small value of the effective figure of merit of commercial thermoelectric modules [45].

On the other hand, the hydraulic power needed to move a volumetric flow rate $\dot{V}$ of air through the plate-fin heat sink read [26]

$$P_{hy} = \dot{V}\Delta p \tag{17}$$

and, therefore, the maximum net output power that could be extracted by the TEG system here analyzed was

$$P_n = P_{TEG} - \frac{P_{hy}}{\Xi} \tag{18}$$

where Ξ was the fan efficiency (≤ 1), and the TEG generated power P_{TEG} was calculated at maximum conditions (Eq. (16)).

In case of assuming a perfectly efficient fan (i.e., Ξ = 1), and neglecting head losses in conduits other than those taken into account in Eq. (1) for the hydraulic power P_{hy}, the term P_{hy}/Ξ in Eq. (18) corresponds to the minimum external power required to drive the flow through the heat sink. Under these assumptions, P_n would become an upper limit of the actual net output power of the TEG design. It must be noted that the present study only focused on the output power rather than on the efficiency. Thus, the purpose was to maximize Eq. (18) by varying the design of the plate-fin heat sink.

3. Experimental test

The experimental set up used to validate the numerical model consisted of an open-circuit wind tunnel with a rectangular steel tube 0.5 m long with an inner square cross-section of 41 × 41 mm (45 × 45 mm outer cross-section with 2 mm wall thickness). A contraction cone at the inlet guided the outside air to flow into the square-section duct. At the end of this rectangular tube, there was an expansion cone that connected with a 1 m long PVC pipe of 152 mm inner diameter. Finally, at the end of this circular duct, a Hella 24 V DC fan aspirated the flow through all the system. Honeycombs were inserted inside both contraction and expansion cones in order to correctly redirect the flow (see Fig. 2a).

The test zone was located at the middle of the rectangular duct, with a 41 × 41 mm rectangular hole at its base in which the heat sink (#1 in Fig. 2b) was introduced. The validation procedure was carried out with an aluminum plate-fin heat sink with geometrical dimensions listed in Table 1. At the end of Section 4, experimental data obtained with a plate-fin heat sink with dimensions similar to those calculated for the optimum design are presented.

A TEG module (H-199–14-06-L2, Crystal ltd) was located in contact with the aluminum heat sink but just outside the rectangular duct (#2 in Fig. 2b). The TEG module dimensions were 40 × 40 mm (hot and cold surface areas), and 3.3 mm high. Its nominal specifications of voltage, current and output power were 4.50 V, 2.41 A and 10.85 W, respectively, at matched load resistance (1.86 Ω) with hot and cold side temperatures equal to 150 °C and 50 °C, respectively. These conditions corresponded to a heat transfer rate equal to 258.5 W. However, at the same hot side temperature, the nominal output power at 45 °C temperature difference between both hot and cold sides reached 2.5 W only (see supplementary material). Below the TEG, a slab 3 mm thick of ceramic glass with known heat conductivity (≈1.35 W m^{-1} K^{-1}; MACOR, Corning Inc.) with surface area equal to 40 × 40 mm (#3 in Fig. 2b) was included. The hot side of the ceramic glass was in contact with an aluminum rectangular block with surface area equal to 40 × 40 mm and 40 mm high (#4 in Fig. 2b), whose bottom surface was in contact with an electronically controlled hot plate (COMBIPLAC, Selecta) (#6 in Fig. 2b) that allowed to keep its temperature constant. Type K thermocouples (accuracy ± 1.5 °C) 0.25 mm thick were located at the center of all contact surfaces. Each thermocouple was inserted within a slot made in a 0.25 mm thin sheet of brass of 40 × 40 mm surface area located in between the contact surfaces so as to provide a uniform flat surface in these interfaces. Two M5 bolts fitted to angle steel bars (#7 and # 8 in Fig. 2b-c) clamped the system, being packed from the rectangular tube to the hot plate. In order to reduce heat losses to the ambient, the sides of this packed system were surrounded by calcium silicate plates 50 mm thick with very low thermal conductivity (<0.08 W m^{-1} K^{-1} at 200 °C; FTP1000, Alfran) (#5 in Fig. 2b). The environmental temperature (i.e., the temperature of the incoming air) was also measured with a type K thermocouple. All temperature data were acquired with a NI 9211 module of National Instruments and analyzed with LabView software (accuracy ± 1.3 °C). The electrical circuit consisted of a rheostat of 5 Ω (10 W) manually operated connected to both terminals of the TEG module. TEG voltage and current were also monitored with National Instruments modules NI 9215 and NI 9227, respectively (accuracies ±(0.00853 + 0.2 %) V for voltage, and

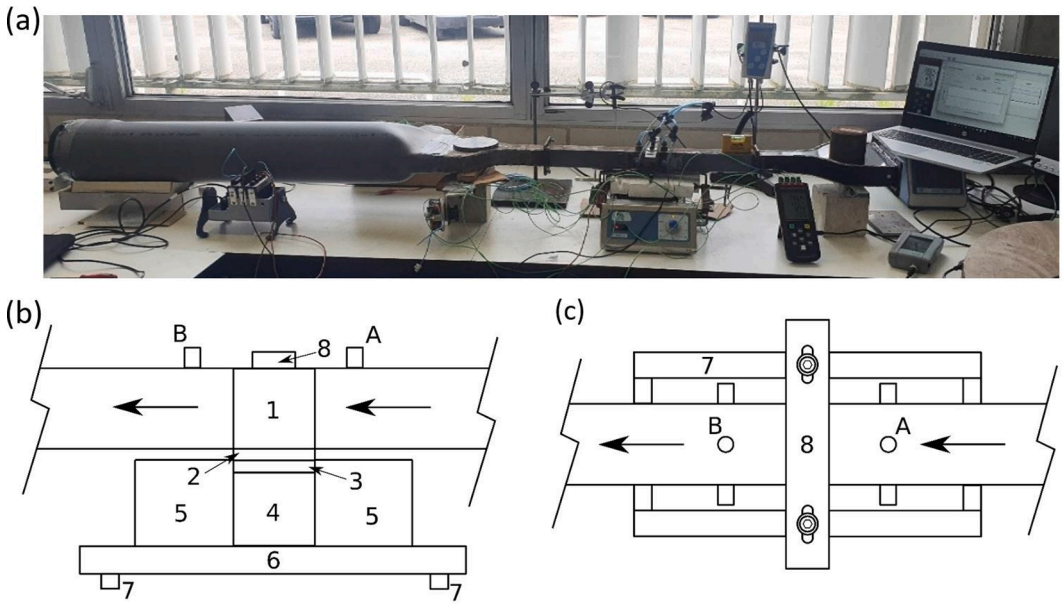

Fig. 2. (a) Picture of the experimental set up, (b) schematic half-section view of the test zone, (c) and schematic upper view of the test zone. In (b)-(c), the elements listed are heat sink (1), TEG (2), ceramic slab (3), aluminum block (4), insulating material (5), hot plate 6, angle steel bars to clamp the system (7, 8), location of the differential pressure sensor (A, B). For details, see text.

Table 1
Geometrical dimensions of the aluminum plate-fin heat sink shown in Fig. 1.

Parameter	Variable	Units	Value
Heat sink width	W	m	41.0×10^{-3}
Heat sink length	L	m	40.5×10^{-3}
Fin height	H	m	36.0×10^{-3}
Base height	b	m	4.0×10^{-3}
Fin thickness	t	m	1.3×10^{-3}
Fin-to-fin distance	d	m	2.0×10^{-3}
Number of fins	n		13

$\pm(0.0127 + 0.37\ \%)$ A for current).

The pressure drop through the plate-fin heat sink was acquired by means of a differential pressure sensor (SDP610-125PA, Sensirion AG; accuracy $\pm(0.1 + 3\ \%)$ Pa) connected to a junction of three probes located 10 mm upstream and 10 mm downstream of the heat sink (A and B in Fig. 2b-c). The average air velocity was measured with a hot-wire anemometer (VELOPORT 2.0, E + E Elektronik Ges.m.b.H; accuracy $\pm(0.04 + 1\ \%)$ m s^{-1}) by averaging data obtained after inserting the probe at 10 different depths in the inlet contraction cone. Experimental data were repeated three times to ensure repeatability.

The experimental procedure consisted of 1) setting a fixed voltage for the fan, 2) setting a constant temperature at the hot plate in order to reach a $T_{TEG,h} \approx 150$ °C (this was the nominal temperature at $T_{TEG,h}$ according to manufacturer's datasheet), 3) adjusting the rheostat until reaching the maximum TEG output power, 4) monitoring all data for a minimum period of 30 s and with>60 samples, 5) opening the electrical circuit, wait until the temperatures stabilize and measure the open circuit voltage, 6) repeating steps 1) to 5) for different fan voltages (i.e., fluid flow velocities).

Data uncertainties ε_t were calculated as

$$\varepsilon_t = \sqrt{\varepsilon_e^2 + \varepsilon_s^2} \tag{19}$$

where ε_e was the uncertainty due to the measurement equipment (accuracies pointed out above) and ε_s was the uncertainty of the data series acquired, being

$$\varepsilon_s = \pm z_{0.025} \frac{\sigma_{st}}{\sqrt{N}} \tag{20}$$

where $z_{0.025}$ was the value for a 95 % confidence interval (=1.960), σ_{st} the standard deviation of the data series and N the number of samples.

Open circuit voltages divided by the temperature differences at both hot and cold TEG sides provided the effective value of the Seebeck coefficient, with an average value equal to $\alpha = 0.0595$ V K^{-1} (standard deviation equal to 0.9×10^{-3} V K^{-1}). The effective thermal resistance of the TEG module was calculated from the manufacturer's datasheet at the nominal point ($T_{TEG,h} = 150$ °C, $T_{TEG,c} = 50$ °C and maximum power), being $R_{cd,TEG} = 0.387$ K W^{-1}. The effective internal electrical resistance of the TEG was assumed to be 2.96 Ω (standard deviation equal to 0.12 Ω) obtained from applying matching conditions with the load resistance at maximum power, and averaging the results for all cases. For simplicity, all the previous parameters were assumed constant when used in the numerical model.

The pressure drop data through the aluminum plate-fin heat sink as a function of the flow velocity in the rectangular tube are shown in Fig. 3. Results from the analytical model detailed in Section 2 are also depicted. Note that predictions correctly reproduced the experimental values, supporting the validity of the hydraulic model.

On the other hand, Fig. 4 shows the convective thermal resistance $R_{cv,HS}$ of the plate-fin heat sink, and the total thermal resistance R_t of the experimental set up (ceramic plus TEG module plus plate-fin heat sink in Fig. 1). Here, the experimental $R_{cv,HS}$ and R_t values were obtained from the measured temperatures and the calculation of the heat transfer rate Q through the ceramic slab of known thermal conductivity, so no experimental fin efficiency term values were assumed (i.e., laboratory data of $R_{cv,HS}$ and R_t were obtained from $\Delta T/Q$ with ΔT the observed temperature difference in the corresponding elements in Fig. 1a). The thermal model predicted larger values of the convective thermal resistance than the measured ones, especially at low flow rates. This difference might have been caused by heat transfer losses due to the contact of the fin tips with the duct in the experimental set up. At low air flow rate values, the relevance of this thermal bridge increased, and observations might indicate a substantially more efficient heat sink than that predicted from the model as it assumed adiabatic fin tips. This effect

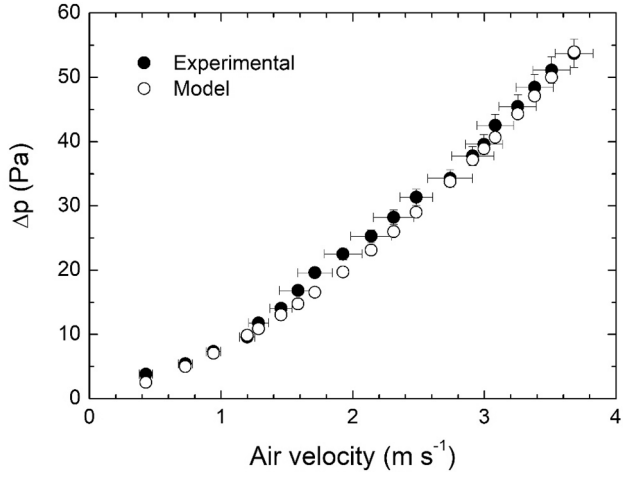

Fig. 3. Experimental and modeled pressure drop through the aluminum plate-fin heat sink detailed in Table 1 as a function of the average velocity of the incoming flow.

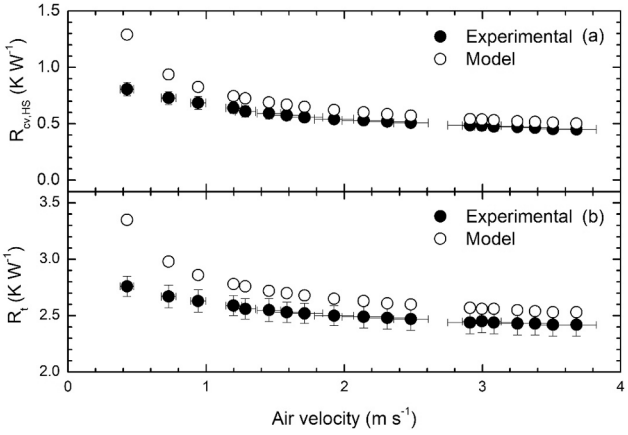

Fig. 4. Experimental and modeled (a) convective thermal resistance of the plate-fin heat sink detailed in Table 1, and (b) total thermal resistance of the ceramic plus TEG plus heat sink system shown in Fig. 1a as a function of the average velocity of the incoming flow.

reduced as forced flow increased, and both measured and simulated data tended to convergence.

Finally, the maximum TEG output power P_{TEG} as well as the maximum net output power of the whole TEG system P_n as a function of the incoming flow velocity are shown in Fig. 5. For constant air flow rate and heat sink geometry, the maximum in P_n was achieved when the electrical load resistance was adjusted to maximize P_{TEG} since P_{hy} was independent of the thermal and electrical circuits when using constant fluid properties in the numerical model. The model remarkably predicted the experimental data for both variables. The point at maximum output power at Fig. 5 had a hot side temperature equal to 141 °C and a temperature difference between both sides equal to 46 °C. Though these conditions were not specified in the modules' datasheet, an output power around 2 W would be expected from listed values (see supplementary material). The reason of having a more reduced output power value (0.84 W) (and, as a consequence, a low value of net output power) in the laboratory analysis may come from not reaching the contact pressure required for the TEG module (1.2 MPa). This is why the model applied a Seebeck coefficient based on the experimental data obtained under open circuit conditions (as explained above), and not based on the manufacturer's datasheet.

P_n reached a maximum at intermediate volumetric flow rates since the hydraulic power P_{hy} increased in a quadratic (cubic) form in terms of $\dot{V}$ for laminar (turbulent) flows, and the temperature difference across the TEG (and, thus, P_{TEG}) asymptotically tended to a threshold value as $\dot{V}$ increased. This maximum was labelled as P_{nmax,vR_L} since it corresponded to the maximum net output power with unconstrained values of air flow velocity v and electrical load resistance R_L, with constant values of the geometrical dimensions of the aluminum heat sink (as in Table 1). In Fig. 5b, the fan efficiency was assumed to be $\Xi = 1$, aiming to obtain an upper bound of the net available output power P_n. Lower efficiency values did not modify the agreement between predictions and measurements since Ξ equally affected both experimental and numerical P_{hy}/Ξ terms in Eq. (18). However, it affected the quantitative values of P_{nmax,vR_L} achieved, being lower than that reported in Fig. 5b.

4. Numerical results

The previous section confirmed the validity of the numerical model to reproduce the experimental data of the aluminum plate-fin heat sink with dimensions listed in Table 1. In this section, the model was applied to determine the main design parameters of the heat sink (i.e., t and d, and, consequently n) that led to an optimal value of the available output

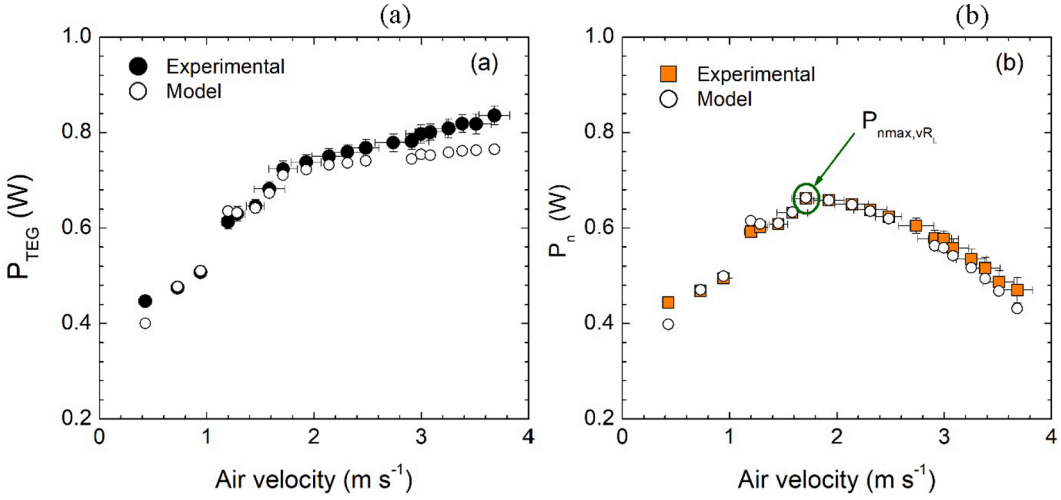

Fig. 5. (a) Maximum TEG output power obtained varying the electrical load resistance P_{TEG}, and (b) net output power P_n at P_{TEG} conditions as a function of the average velocity of the incoming flow for the aluminum plate-fin heat sink design detailed in Table 1. P_{nmax,vR_L} is the maximum P_n value with unconstrained values of incoming air flow v and electrical load resistance R_L, with all other parameters as in Table 1.

power P_n. All other heat sink geometrical dimensions were kept constant (width W, length L, fin height H and base height b) with values equal to those in Table 1 (except in Fig. 14 as mentioned later) in order to study forced convection without bypass in the duct under study. The numerical model detailed in Section 2 was not valid in cases in which the heat sink did not occupy the entire duct cross-sectional area [46]. Unless otherwise stated, the hot side TEG temperature $T_{TEG,h}$ and the environment temperature T_a were fixed to 160 °C and 24 °C, respectively, being similar to those found in the experimental set up detailed in Section 3.

4.1. Unconstrainedd,vandR$_L$

Fig. 6 depicts the maximum net output power obtained for different values of the fin-to-fin distance d and with other geometrical heat sink dimensions kept fixed as in Table 1 when varying the electrical load resistance and the volumetric flow rate through the plate-fin heat sink. Note that the d values were discrete since the dimensions of the heat sink were forced to match the duct inner width. Thus, each point in Fig. 6 made reference to heat sinks with different number of fins. In particular, $n = 13$ for the case marked as tested ($d = 2 \times 10^{-3}$ m, Section 3), whereas $n = 19$ ($d = 0.9 \times 10^{-3}$ m) at the point of maximum net output power P_{nmax,dvR_L} (=0.93 W). Once at P_{nmax,dvR_L} the decrease in power was more pronounced towards smaller d distances than towards greater ones. This was caused because small d distances for equal fin thickness t are equivalent to high number of fins and, hence, to higher hydraulic pressure drop values (and, hence, higher P_{hy}) for the same value of volumetric flow rate.

Values of both P_{TEG} and P_{hy} when the net output power was maximum for heat sinks for unconstrained values of v and R_L as a function of the fin-to-fin distance d are detailed in Fig. 7. The dimensions that provided a higher P_{TEG} value ($n = 20$, $d = 0.8 \times 10^{-3}$ m) were not those giving the maximum net output power ($n = 19$, $d = 0.9 \times 10^{-3}$ m). The contribution of the pressure drop term P_{hy}, in comparison with that of P_{TEG}, was very high at small d distances or, equivalently, at high number of fins. Note that neither the maximum of P_{TEG} (attained at the maximum achievable flow rate) nor the minimum of P_{hy} (obtained at zero flow rate) are represented in Fig. 7. This is because all net output power values shown in this section assumed flow rate values through the plate-fin heat sink that maximized P_n only.

4.2. Unconstrained t, d, v and R$_L$: Optimal case

Contour values of maximum net output power P_{nmax,vR_L} with unconstrained values of R_L and v as a function of both fin thickness t and fin-to-fin distance d are represented in Fig. 8. The number of cases used in Fig. 8 was determined by the constraint applied on the plate-fin heat sink dimensions of matching the inner tube width. Thus, not all the combinations of fin thickness and fin-to-fin gap in Fig. 8 were physically possible. Both parameters are linked through the number of fins n, which is a discrete variable. The cases employed in Fig. 8 were obtained with heat sink dimensions varying at intervals of 0.01×10^{-3} m for the fin thickness and using heat sinks with number of fins n ranging from 8 to 2000. For all these cases, the flow rate was chosen so as to maximize the net output power P_n. Thus, for example, P_{nmax,vR_L} values illustrated in Figs. 6 and 7 corresponded to values at $t = 1.3 \times 10^{-3}$ m in Fig. 8. For a constant fin thickness, the fin-to-fin distance that provided the maximum net output power was on the order of 0.9×10^{-3} m. For a fixed value of fin-to-fin distance, the fin thickness that gave the maximum net output power varied, decreasing as fin spacing decreased. Note that the fin spacing had a larger influence on the net output power than the fin thickness.

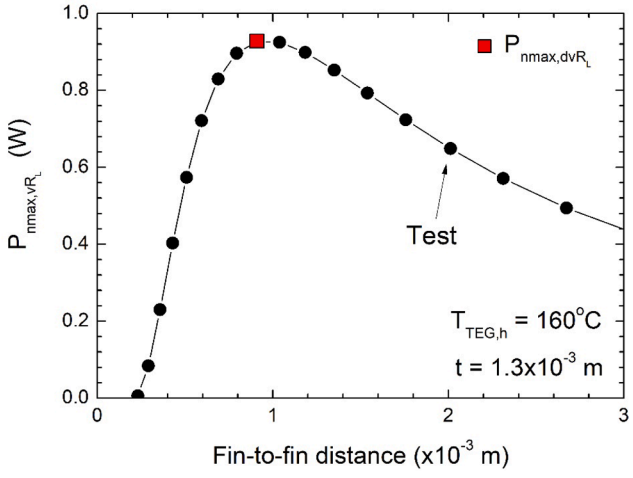

Fig. 6. Maximum net output power of a heat sink with varying v and R_L (P_{nmax,vR_L}) as a function of the fin-to-fin distance d with all other geometrical dimensions as in Table 1. The maximum value for any d is also reported (P_{nmax,dvR_L}). All cases withT_a = 24 °C.

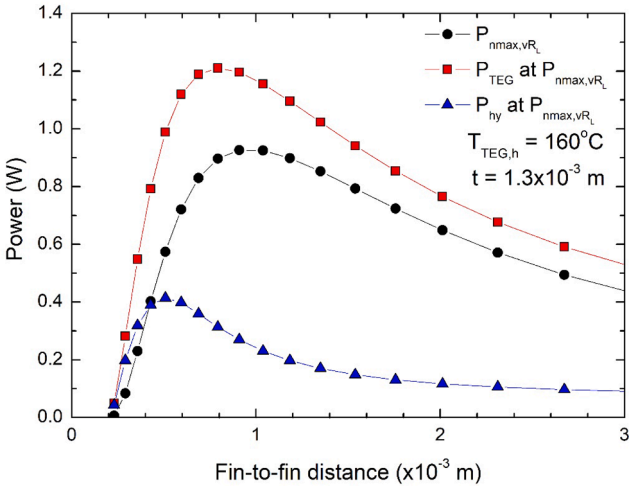

Fig. 7. TEG output power P_{TEG} and hydraulic loss P_{hy} at conditions of maximum net output power P_n reported in Fig. 6.

The optimal net output power P_{nopt} was defined as the plate-fin heat sink configuration that provided the maximum value of P_n when varying t, d, v and R_L. It corresponded to the maximum of P_{nmax,vR_L} found in Fig. 8, reached at $t = 0.44 \times 10^{-3}$ m and $d = 0.87 \times 10^{-3}$ m.

Selected values of Fig. 8 are represented in Fig. 9 (data for heat sink geometries at intervals of fin thickness equal to 0.05×10^{-3} m starting at $t = 0.1 \times 10^{-3}$ m) as a function of the number of fins n. The P_{nopt} value obtained with $t = 0.44 \times 10^{-3}$ m and $d = 0.87 \times 10^{-3}$ m required 32 fins.

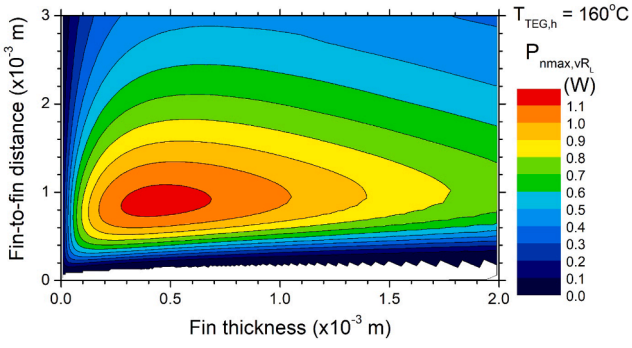

Fig. 8. Contours of maximum net output power with unconstrained v and R_L (P_{nmax,vR_L}) as a function of the fin thickness t and the fin-to-fin distance d for$T_{TEG,h}$ = 160 °C andT_a = 24 °C. All other geometrical dimensions as in Table 1.

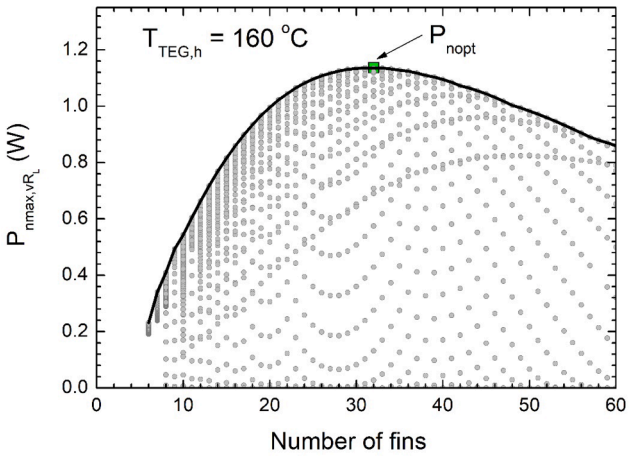

Fig. 9. Maximum net output power cases with unconstrained v and R_L (P_{nmax,vR_L}) for different values of fin thickness and fin-to-fin distance as a function of the number of fins n for $T_{TEG,h} = 160$ °C and $T_a = 24$ °C. The optimal ($P_{nopt} = 1.14$ W) was found at $n = 32$ with fin thickness $t = 0.44 \times 10^{-3}$ m and fin-to-fin distance $d = 0.87 \times 10^{-3}$ m. The line indicates the Pareto front, and corresponds to the $P_{nopt,n}$ values.

The optimal value almost doubled the net output power of a heat sink with the geometrical dimensions of the tested one in Section 3. The frontier of the maximum net output power for a fixed value of number of fins did not vary as more heat sinks designs were included in the analysis, which was done by increasing the refinement of the fin thickness interval applied to obtain Fig. 9. This Pareto front indicated the maximum allowable net output power value P_{nmax,vR_L} for all heat sinks that had the same number of fins n. This maximum, referred to as $P_{nopt,n}$, was attained with different heat sink configurations. However, it changed when the temperature conditions at the TEG hot side varied as discussed next.

4.3. Optimal net power output as a function of the hot side temperature

The normalized values of the maximum net output power for a constant n ($P_{nopt,n}$) with respect to the optimal net output power P_{nopt} are shown in Fig. 10 for different $T_{TEG,h}$ temperatures. Values of P_{nopt} were 0.11 W, 0.47 W, 1.14 W, 2.15 W for $T_{TEG,h} = 80$ °C, 120 °C, 160 °C and 200 °C, respectively. As the TEG hot side temperature decreased, the $P_{nopt,n}/P_{nopt}$ curve behaved more abruptly and with a peak that shifted towards heat sinks with smaller number of fins. Therefore, the selection of the correct heat sink is critical for low temperature applications, where the effect of choosing an incorrect design may easily lead to working conditions far from the optimal ones. Conversely, at high temperatures, the variation of the $P_{nopt,n}/P_{nopt}$ ratio was not so severe when the number of fins increased. Besides, the reduction of the maximum net output power $P_{nopt,n}$ found by decreasing the number of fins of the optimal heat sink design P_{nopt} was very abrupt and almost equal for all the hot side temperatures analyzed. Thus, the design of the plate-fin heat sink should avoid very low number of fins.

Fin thickness values that provided the maximum net output power for a given number of fins are shown in Fig. 11 for different TEG hot side temperatures. Since both scales are logarithmic, the fin thickness that provided the maximum net output power for a given number of fins n followed $t_{P_{nopt,n}} = an^b$ with $a \approx 0.10 \times 10^{-3}$ m (a value slightly dependent on $T_{TEG,h}$) and $b \approx -1.55$ (almost independent of $T_{TEG,h}$). The few scattered points in Fig. 11 observed at low number of fins corresponded to turbulent conditions in comparison with all other points in which the flow regime between the heat sink channels was laminar.

Values of the optimal net output power P_{nopt} for different temperatures at the TEG hot side are shown in Fig. 12a. Differences between the TEG power generation and P_{nopt} in Fig. 12a corresponded to the hydraulic power divided by the fan efficiency required to drive the flow through the heat sink. Since the latter ignored any pressure drop through additional conduits and used a fan efficiency equal to 1, the P_{nopt} values illustrated in Fig. 12a were upper limits of the available net power extracted from the device.

The convective thermal resistance $R_{cv,HS}$ and the air flow velocity v at optimal conditions as a function of the TEG hot side temperature are represented in Fig. 12b. The condition of maximum net output power in the experimental analyses, Section 3, had a $R_{cv,HS}$ value 33 % greater and an air flow velocity v value 55 % smaller than the optimal ones. Fig. 13 shows the values of fin thickness, fin-to-fin distance and number of fins that produced the optimal net output power cases illustrated in Fig. 12. The optimal found in Figs. 8 and 9 are the points at $T_{TEG,h} = 160$ °C in Fig. 13. The fin thickness of the optimal configuration was almost invariable through the whole range of hot side temperatures, with a very slight trend to decrease as $T_{TEG,h}$ increased. By contrast, the fin spacing of the optimal configuration substantially varied as a function of $T_{TEG,h}$,

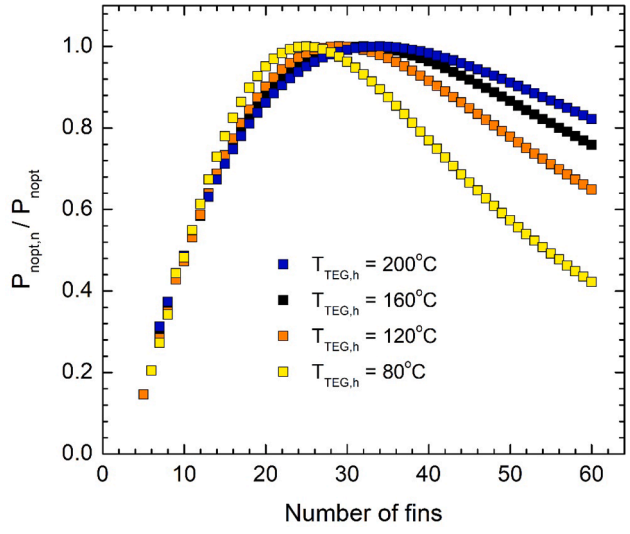

Fig. 10. Ratio of the maximum net output power for a fixed number of fins $P_{nopt,n}$ to the optimal net output power P_{nopt} for different values of $T_{TEG,h}$. All cases use $T_a = 24$ °C and geometrical parameters other than fin thickness, fin-to-fin distance, and number of fins, as in Table 1.

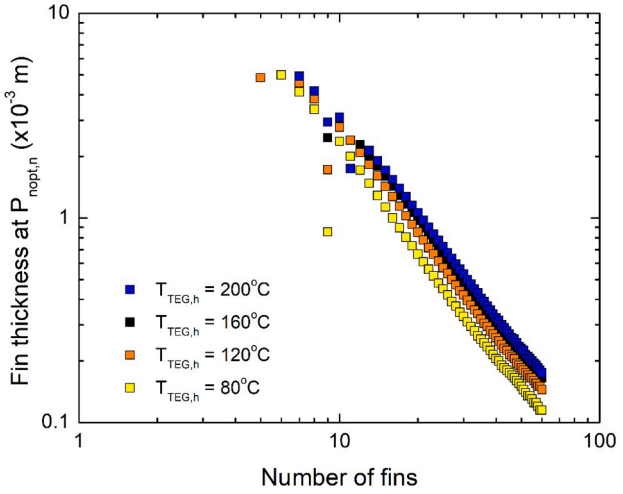

Fig. 11. Fin thickness at the maximum net output power for fixed number of fins $P_{nopt,n}$ as a function of the number of fins n for different values of $T_{TEG,h}$. All cases use $T_a = 24$ °C and geometrical parameters other than fin thickness, fin-to-fin distance, and number of fins, as in Table 1.

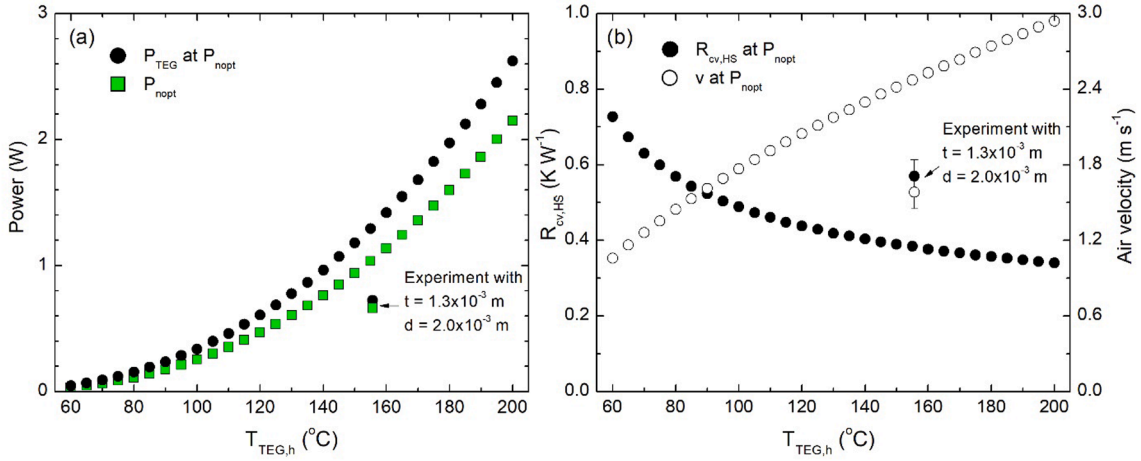

Fig. 12. (a) Optimal net output power P_{nopt} and TEG output power at P_{nopt}, and (b) convective thermal resistance and air flow velocity both at P_{nopt} for different values of $T_{TEG,h}$. All cases useT_a = 24 °C and geometrical parameters other than fin thickness, fin-to-fin distance, and number of fins, as in Table 1. For comparison purposes, the experimental values at P_{nmax,vR_L} of Fig. 5 have been included.

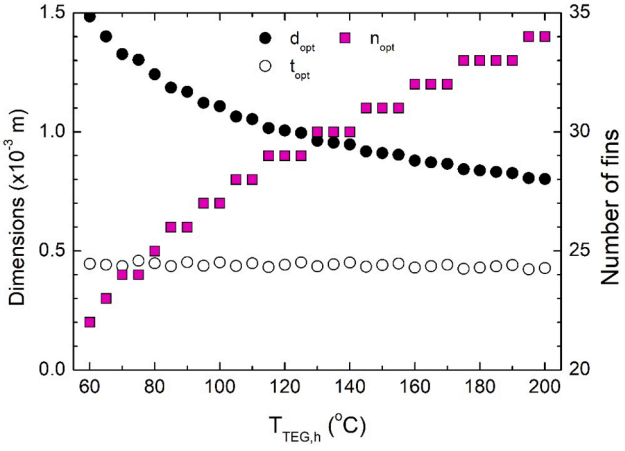

Fig. 13. Fin thickness t_{opt}, fin-to-fin distance d_{opt} and number of fins n_{opt} at the optimal net output power P_{nopt} for those cases shown in Fig. 12.

decreasing as the temperature increased. This was caused by the need of enhancing the heat transfer to the ambient air as the base plate became hotter, which was achieved by including more fins in the heat sink (Fig. 13). Since, as it was pointed out previously, the fin spacing had a larger influence on the net output power than the fin thickness, d_{opt} varied more than t_{opt} as a function of temperature.

Efficiency values (power generation divided by heat transfer rate) were below 0.8 % for the TEG conversion in the $T_{TEG,h}$ = 160 °C case, reducing up to 0.6 % when using the net output power value instead of the TEG power generation one (i.e., efficiency related to the net output power). The trend of the efficiency values was to increase with $T_{TEG,h}$ ranging from 0.2 % ($T_{TEG,h}$ = 60 °C) to 1.1 % ($T_{TEG,h}$ = 200 °C). The efficiencies computed with the net output power P_n instead of with P_{TEG} were between 20 % and 30 % smaller.

From the above, the optimal conditions of the device analyzed in Section 3 required a heat sink with fin thickness on the order of 0.5 × 10^{-3} m and fin-to-fin distance on the order of 1 × 10^{-3} m. In comparison, the maximum heat transfer design found by Bar-Cohen et al. [17] in a forced convection heat sink with a small air flow pumping power (0.2 W; similar to the experimental values obtained in Section 3) corresponded to a fin thickness t = 0.57 × 10^{-3} m. At larger heat transfer loads (Q = 30 W), the optimal value proposed by Culham and Muzychka [16] used t = 0.40 × 10^{-3} m. This fin thickness value increased to t = 1.0 × 10^{-3} m (with d = 1.6 × 10^{-3} m) when simultaneously optimizing the manufacturing costs in multi-objective analysis [18]. Since, here, the goal function was the maximum net output power only, the results obtained were in agreement with those previously found [16–17].

Are these dimensions feasible for mass production with current

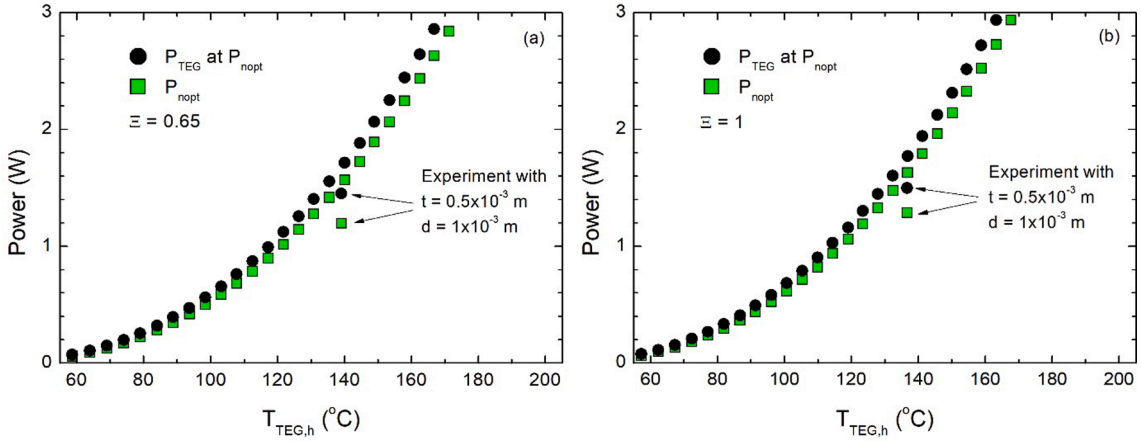

Fig. 14. Optimal net output power P_{nopt} and TEG output power at P_{nopt} for different values of $T_{TEG,h}$ using conditions of the copper folded heat sink with fan efficiency of (a) 65 % and (b) 100 %. Experiments show P_{nmax,vR_L} and P_{TEG} at P_{nmax,vR_L} conditions. All cases useT_a = 22 °C.

manufacturing techniques? From information gathered from several manufacturers, the main methods employed in manufacturing heat sinks are extrusion, forging, bonding, folding and skiving. A review of the products offered by several companies led to the information detailed in Table 2 [47–50], where the fin-to-fin distance for extrusion, forged, and bonded heat sinks was estimated form the fin height/fin gap ratio found in the datasheets using a fin height equal to 36×10^{-3} m (as in Table 1). Current commercial ranges of fin thickness and fin spacing per material and manufacturing method reveal that folding and skiving techniques may produce heat sinks with the required fin density for the optimal configuration. The folding method is more cost-effective than skiving, although it includes a new contact thermal resistance in the system consisting of that between the base and the fins. Since this contact resistance is expected to be low, folded heat sinks are recommended in order to achieve the optimum of the net output power of single-module TEG systems under forced convection.

To determine the validity of the model predictions, a further experimental analysis was carried out. A folded heat sink was custom-made with geometrical dimensions similar to those expected for the optimal configuration previously found: fin thickness $t = 0.5 \times 10^{-3}$ m, fin-to-fin distance $d = 1.0 \times 10^{-3}$ m and number of fins $n = 29$ (see Fig. 13 for $T_{TEG,h}$ ranging from 120 °C to 140 °C). Other dimensions were fin height $H = 36.6 \times 10^{-3}$ m, length $L = 40.0 \times 10^{-3}$ m, and width $W = 39.6 \times 10^{-3}$ m. The folded heat sink was made of copper due to manufacturing requirements.

For the folded heat sink, Fig. 14 shows the optimal net output power as a function of the hot side TEG temperature predicted by the model assuming fan efficiencies of $\Xi = 0.65$ (Fig. 14a) and $\Xi = 1$ (Fig. 14b). The values in Fig. 14b did not match those of Fig. 12 since the heat sink had different physical properties and the TEG module was replaced by a new unit of the same model (H-199–14-06-L2, Crystal ltd). The effective Seebeck coefficient for this module was obtained from dividing open circuit voltages by the temperature differences at TEM's sides, as in Section 3. The average value of the effective Seebeck coefficient reached $\alpha = 0.0679$ V K^{-1} (14 % higher than that used with the aluminum heat sink in Section 3). In Fig. 14, the experimental data obtained with the folded heat sink refer to values measured at the maximum net output power (i.e., as P_{nmax,vR_L} in Fig. 5).

In comparison with the optimal prediction, the maximum experimental net output power and the TEG output power at that maximum for the new heat sink were 20 % and 15 % lower, respectively. For these conditions, the thermal resistance was 11 % higher and the air flow velocity was 15 % lower than the optimal predictions. Part of this discrepancy may be explained by the fact that, for the conditions of the new folded heat sink, the analytical model predicted an optimum geometry with fin thickness $t_{opt} = 0.32 \times 10^{-3}$ m, fin-to-fin distance $d_{opt} = 0.98 \times 10^{-3}$ m, and $n_{opt} = 31$ fins. This configuration was slightly different than that tested, which was manufactured reproducing the recommendations extracted from Fig. 13. The experimental results for the folded heat sink were much closer to the model optimal than for the aluminum heat sink case (Fig. 12), since there the differences between the geometrical dimensions tested and those of the optimal one were greater. Similar conclusions were extracted by assuming a 65 % fan efficiency, though with lower performance for the net output power since more energy was diverted to feed the fan (Fig. 14a). Note that the exact values of the optimal fin thickness t and the fin-to-fin distance d depended on the TEG performance characteristics, especially on both the effective Seebeck coefficient and the effective thermal resistance. However, the methodology here developed can be easily applied to new TEG conditions, as well as to different geometrical dimensions of the plate-fin heat sink (H, L, and W).

Table 2
Geometrical parameters of heat sinks currently offered by several companies [47–50].

Manufacturing technique	Material	Fin thickness ($\times 10^{-3}$ m)	Fin-to-fin distance ($\times 10^{-3}$ m)
Extrusion	Al	> 0.5	> 1.6
Forging	Al/Cu	> 0.7	> 1.4
Bonding	Al/Cu	> 0.5	> 1.2
Folding	Al/Cu	> 0.2	> 0.5
Skiving	Al/Cu	> 0.1	> 0.1

5. Conclusions

An analytical model of the electric, thermal, and hydraulic behavior of a single commercial thermoelectric generator module with a plate-fin heat sink under forced convection was developed. Experimental data obtained under different flow rates were used to validate the model output. Laboratory results showed that, for a constant temperature value at the hot source, there existed a cooling flow rate value in which the net output power was maximum. These conditions were well reproduced by the numerical model.

An analysis of the effect of modifying the geometrical dimensions of the heat sink with a fin height fixed to match the dimensions of the conduit were:

a) net output power results were more insensitive to changes in fin thickness than in fin-to-fin distance.
b) for a constant temperature value at the thermoelectric hot side, a reduction in the number of fins with respect to the optimal number had strong effects on the reduction of the maximum net output power.
c) the fin thickness t that produced the maximum net output power followed a power law function as a function of the number of fins, $t = an^b$ with a coefficient b independent of the hot side temperature.
d) the optimal heat sink design (maximum net output power among all of the geometrical configurations of the heat sink) predicted by the model varied as a function of the TEG effective properties and heat sink physical properties. For the two heat sinks experimentally analyzed (copper folded; aluminum extruded), the optimal conditions were predicted to occur at fin thicknesses equal to 0.32×10^{-3} m and 0.44×10^{-3} m, respectively, being almost independent of the hot side temperature, and at fin spacing on the order of 1×10^{-3} m, reducing as the hot side temperature increased. These dimensions are better obtained with folded fin heat sinks that appear as the most suitable products to cope with the high fin densities required for the optimal designs. The experiment with a copper folded heat sink produced a net output power of 1.29 W (20 % lower than the optimal predicted), whereas the aluminum extruded one gave 0.66 W only (36 % lower than the optimal predicted).

The values of the optimal fin thicknesses predicted by the model were similar to those reported in previous studies of heat transfer optimization in plate-fin heat sinks [16–17,21]. In comparison, a TEG was also included here, which led to a comprehensive model of a single TEG module. This model may be used as a design tool for these low power generation systems. However, only devices that comply with the limitations of the method developed must be taken into account. In this case, a successful prediction requires reliable input information of the effective TEG properties, which are suggested to be extracted from experimental data in relevant environment.

Declaration of Competing Interest

The authors declare that they have no known competing financial interests or personal relationships that could have appeared to influence the work reported in this paper.

Data availability

Data will be made available on request.

Acknowledgements

This work was partially funded by the University of Girona under grant MPCUdG2016-4. The authors thank the Flemish Fund for Scientific Research FWO for the funding of the research exchange between the University of Ghent and the University of Girona. The authors gratefully acknowledge the technical support provided by Sergi Saus and Jordi Vicens. Martí Roca and Louis Maenhout provided very helpful assistance in the experimental tests.

References

[1] S.M. Pourkiaei, M.H. Ahmadi, M. Sadeghzadeh, S. Moosavi, F. Pourfayaz, L. Chen, M.A. Pour Yazdi, R. Kumar, Thermoelectric cooler and thermoelectric generator devices: a review of present and potential applications, modeling and materials, Energy 186 (2019), 115849, https://doi.org/10.1016/j.energy.2019.07.179.
[2] O.H. Ando Junior, A.L.O. Maran, N.C. Henao, A review of the development and applications of thermoelectric microgenerators for energy harvesting, Renew. Sustain. Energy Rev. 91 (2018) 376–393, https://doi.org/10.1016/j.rser.2018.03.052.
[3] Gentherm Global Power Technologies, Calgary, Canada. Available from: <http://www.genthermglobalpower.com/> Accessed November 20, 2019.
[4] Y. Huang, D. Xu, J. Kan, W. Li, Study on field experiments of forest soil thermoelectric power generation devices, PLoS ONE 14 (8) (2019) e0221019, doi: 10.1371/journal.pone.0221019.
[5] Y. Cai, Y. Wang, D. Liu, F.-Y. Zhao, Thermoelectric cooling technology applied in the field of electronic devices: updated review on the parametric investigations and model developments, Appl. Therm. Eng. 148 (2019) 238–255, https://doi.org/10.1016/j.applthermaleng.2018.11.014.
[6] L. Lin, Y.-F. Zhang, H.-B. Liu, J.-H. Meng, W.-H. Chen, X.-D. Wang, A new configuration design of thermoelectric cooler driven by thermoelectric generator, Appl. Therm. Eng. 160 (2019), 114087, https://doi.org/10.1016/j.applthermaleng.2019.114087.
[7] R. Kiflemariam, C.-X. Lin, Experimental investigation on heat driven self-cooling application based on thermoelectric system, Int. J. Therm. Sci. 109 (2016) 309–322, https://doi.org/10.1016/j.ijthermalsci.2016.06.001.
[8] A. Martínez, D. Astrain, A. Rodríguez, Experimental and analytical study on thermoelectric self cooling of devices, Energy 36 (2011) 5250–5260, https://doi.org/10.1016/j.energy.2011.06.029.
[9] A. Martinez, D. Astrain, P. Aranguren, Thermoelectric self-cooling for power electronics: Increasing the cooling power, Energy 112 (2016) 1–7, https://doi.org/10.1016/j.energy.2016.06.007.
[10] H.-H. Wu, Y.-Y. Hsiao, H.-S. Huang, P.-H. Tang, S.-L. Chen, A practical plate-fin heat sink model, Appl. Therm. Eng. 31 (2011) 984–992, https://doi.org/10.1016/j.applthermaleng.2010.10.014.
[11] R.W. Knight, J.S. Goodling, D.J. Hall, Optimal thermal design of forced convection heat sinks-Analytical, J. Electron. Packag. 113 (1991) 113, https://doi.org/10.1115/1.2905412.
[12] R.W. Knight, J.S. Goodling, B.E. Gross, Optimal thermal design of air cooled forced convection finned heat sinks-Experimental verification, IEEE Trans. Components Hybrids Manuf. Technol. 15 (5) (1992) 754–760, https://doi.org/10.1109/ITHERM.1992.187765.
[13] P. Teertstra, M.M. Yovanovich, J.R. Culham, Analytical forced convection modeling of plate fin heat sinks, J. Electron. Manuf. 10 (4) (2000) 253–261.
[14] A. Bejan, A.M. Morega, Optimal arrays of pin fins and plate fins in laminar forced convection, J. Heat Transfer 115 (1) (1993) 75–81, https://doi.org/10.1115/1.2910672.
[15] A. Bejan, Entropy Generation Minimization, CRC Press, Boca Raton, 1996.
[16] J.R. Culham, Y.S. Muzychka, Optimization of plate fin heat sinks using entropy generation minimization, IEEE Trans. Compon. Packag. Technol. 24 (2) (2001) 159–165, https://doi.org/10.1109/6144.926378.
[17] A. Bar-Cohen, R. Bahadur, M. Iyengar, Least-energy optimization of air-cooled heat sinks for sustainability-theory, geometry and material selection, Energy 31 (2006) 579–619, https://doi.org/10.1016/j.energy.2005.05.005.
[18] C.-T. Chen, H.-I. Chen, Multi-objective optimization design of plate-fin heat sinks using a direction-based genetic algorithm, J. Taiwan Inst. Chem. Eng. 44 (2013) 257–265, https://doi.org/10.1016/j.jtice.2012.11.012.
[19] S. Gondipali, B. Sammakia, S. Lu, G. Refai-Ahmed, Fin-shape optimization of an impingement-parallel plate heat sink, in: 12th IEEE Intersociety Conference on Thermal and Thermomechanical Phenomena in Electronic Systems, 2010, doi: 10.1109/ITHERM.2010.5501380.
[20] A. Al-Damook, N. Kapur, J.L. Summers, H.M. Thompson, Computational design and optimisation of pin heat sinks with rectangular perforations, Appl. Therm. Eng. 105 (2016) 691–703, https://doi.org/10.1016/j.applthermaleng.2016.03.070.
[21] M. Pragadeesh, M. Shanmugasundaram, C. Balachandar, M. Venkatesan, ANN-GA optimisation of rectangular fin array with closed top plate under forced convection, Progress Comput. Fluid Dynamics 18 (3) (2018) 188–198, https://doi.org/10.1504/PCFD.2018.091702.
[22] Ö. Özdilli, S. Şevik, Effect of channel and fin geometries on a trapeze plate-fin heat sink performance, Proc. Inst. Mech. Eng., Part E: J. Process Mech. Eng. 235 (5) (2021) 1326–1336.
[23] S. Şevik, Ö. Özdilli, Experimental and numerical analysis of the splay impact on the performance of splayed cross-cut fin heat sink, Int. J. Therm. Sci. 170 (2021), 107101, https://doi.org/10.1016/j.ijthermalsci.2021.107101.
[24] A.S. Rattner, T.J. Meehan, Simple analytic model for optimally sizing thermoelectric generator module arrays for waste heat recovery, Appl. Therm. Eng. 146 (2019) 795–804, https://doi.org/10.1016/j.applthermaleng.2018.10.003.
[25] D. Luo, R. Wang, W. Yu, Z. Sun, X. Meng, Modelling and simulation study of a converging thermoelectric generator for engine waste heat recovery, Appl. Therm. Eng. 153 (2019) 837–847, https://doi.org/10.1016/j.applthermaleng.2019.03.060.
[26] M. Comamala, A. Massaguer, E. Massaguer, T. Pujol, Validation of a fuel economy prediction method based on thermoelectric energy recovery for mid-size vehicles, Appl. Therm. Eng. 153 (2019) 768–778, https://doi.org/10.1016/j.applthermaleng.2019.03.004.
[27] W. Liu, Q. Jie, H.S. Kim, Z. Ren, Current progress and future challenges in thermoelectric power generation: from materials to devices, Acta Mater. 87 (2015) 357–376, https://doi.org/10.1016/j.actamat.2014.12.042.
[28] J.H. Meng, X.-X. Zhang, X.-D. Wang, Characteristics analysis and parametric study of a thermoelectric generator by considering variable material properties and heat losses, Int. J. Heat Mass Transf. 80 (2015) 227–235, https://doi.org/10.1016/j.ijheatmasstransfer.2014.09.023.
[29] G.B. Abdallah, S. Beses, H.B. Aissia, J. Jay, Analysis of the effect of a pulsed heat flux on the performance improvements of a thermoelectric generator, Appl. Therm. Eng. 158 (2019), 113728, https://doi.org/10.1016/j.applthermaleng.2019.113728.
[30] A. Martínez, J.G. Vián, D. Astrain, A. Rodríguez, I. Berrio, Optimization of the heat exchangers of a thermoelectric generation system, J. Electron. Mater. 39 (9) (2010) 1463–1468, https://doi.org/10.1007/s11664-010-1291-4.
[31] Y.S.H. Najjar, A. Sallam, Optimum design, heat transfer and performance analysis for thermoelectric energy recovery from the engine exhaust system, J. Electron. Mater. 48 (9) (2019) 5532–5541, https://doi.org/10.1007/s11664-019-07416-y.
[32] N. Kempf, Y. Zhang, Design and optimization of automotive thermoelectric generators for maximum fuel efficiency improvement, Energ. Conver. Manage. 121 (2016) 224–231, https://doi.org/10.1016/j.enconman.2016.05.035.
[33] Y. Wang, C. Wu, Z. Tang, X. Yang, Y. Deng, C. Su, Optimization of fin distribution to improve the temperature uniformity of a heat exchanger in a thermoelectric generator, J. Electron. Mater. 44 (6) (2015) 1724–1732, https://doi.org/10.1007/s11664-014-3527-1.
[34] W. He, R. Guo, H. Takasu, Y. Kato, S. Wang, Performance optimization of common plate-type thermoelectric generator in vehicle exhaust power generation systems, Energy 175 (2019) 1153–1163, https://doi.org/10.1016/j.energy.2019.03.174.
[35] S. Bélanger, L. Gosselin, Multi-objective genetic algorithm optimization of thermoelectric heat exchanger for waste heat recovery, Int. J. Energy Res. 36 (2012) 632–642, https://doi.org/10.1002/er.1820.
[36] D. Ji, Z. Wei, S. Mazzoni, M. Mengarelli, S. Rajoo, J. Zhao, J. Pou, A. Romagnoli, Thermoelectric generation for waste heat recovery: application of a system level design optimization approach via Taguchi method, Energ. Conver. Manage. 172 (2018) 507–516, https://doi.org/10.1016/j.enconman.2018.06.016.
[37] L. Tian, L. Chen, T. Ren, Y. Ge, H. Feng, Optimal distribution of heat exchanger area for maximum efficient power of thermoelectric generators, Energy Rep. 8 (2022) 10492–10500, https://doi.org/10.1016/j.egyr.2022.08.188.
[38] M. Comamala, I.R. Cózar, A. Massaguer, E. Massaguer, T. Pujol, Effects of design parameters on fuel economy and output power in an automotive thermoelectric generator, Energies 11 (2018) 3274, https://doi.org/10.3390/en11123274.
[39] W.-H. Chen, C.-M. Wang, L.H. Saw, A.T. Hoang, A.A. Bandala, Performance evaluation and improvement of thermoelectric generators (TEG): Fin installation and compromise optimization, Energy Conves. Management 250 (2021), 114858, https://doi.org/10.1016/j.enconman.2021.114858.
[40] I. T'Jollyn, T. Pujol, M. De Paepe, A. Massaguer, L. Montoro, Plate fin heat sink modelling and design considerations for thermoelectric generators, Renewable Energy Power Quality J. 15 (2017) 551–556, https://doi.org/10.24084/repqj15.388.
[41] M. Lindstedt, R. Karvinen, Optimization of plate fin arrays with laminar and turbulent forced convection, J. Phys. Conf. Ser. 395 (2012), 012059, https://doi.org/10.1088/1742-6596/395/1/012059.
[42] W.M. Kays, A.L. London, Compact Heat Exchangers, 3rd ed., McGraw Hill, New York, 1984.
[43] M. Comamala, T. Pujol, I.R. Cózar, E. Massaguer, A. Massaguer, Power and fuel economy of a radial automotive thermoelectric generator: experimental and numerical studies, Energies 11 (2018) 2720, https://doi.org/10.3390/en11102720.
[44] E.V. Sempels, F.J. Lesage, Optimization of thermoeletric generators in the presence of heat losses and fluid flows, IEEE Trans. Compon. Packag. Manuf. Technol. 8 (9) (2018) 1573–1580, https://doi.org/10.1109/TCPMT.2018.2864171.
[45] Y. Apertet, H. Ouerdane, C. Goupil, Ph. Lecoeur, Influence of thermal environment on optimal working conditions of thermoelectric generators, J. Appl. Phys. 116 (14) (2014) 144901.
[46] H. Cai, L. Su, Y. Liao, Z. Weng, Numerical and experimental study on the influence of top bypass flow on the performance of plate fin heat exchanger, Appl. Therm. Eng. 146 (2019) 356–363, https://doi.org/10.1016/j.applthermaleng.2018.10.007.

[47] Thermo Cool Corporation, San José, USA. Available from: <https://thermocoolcorp.com/project/>.
[48] Bhoomi Modular Systems Ltd, Gujarat India. Available from: <https://www.bhoomiheatsinks.com/products/bonded-fin-heatsink/bonded-fin-heatsinks/>.
[49] Awind Hardware Ltd, Dongguan City, China. Available from: <https://www.awind-thermal.com/heat-sink/folded-fin-heat-sink/oem-folded-fin-heat-sinks.html>.
[50] Kingka Tech Industrial Limited, Dongguan City, China. Available from: <https://www.kingkatech.com/skived-fin-heat-sink.html>.